



# Self-assembled Ni/NiO impregnated polyaniline nanoarchitectures: A robust bifunctional catalyst for nitrophenol reduction and epinephrine detection

Manigandan Ramadoss<sup>a,b</sup>, Yuanfu Chen<sup>a,c,\*</sup>, Suresh Ranganathan<sup>b</sup>, Krishnan Giribabu<sup>b</sup>, Dhanasekaran Thangavelu<sup>b</sup>, Padmanaban Annamalai<sup>b</sup>, Narayanan Vengidusamy<sup>b,\*\*</sup>

<sup>a</sup> School of Electronic Science and Engineering and State Key Laboratory of Electronic Thin Films and Integrated Devices, University of Electronic Science and Technology of China, Chengdu, 610054, PR China

<sup>b</sup> Department of Inorganic Chemistry, University of Madras, Guindy Campus, Chennai, 600025, India

<sup>c</sup> School of Science and Institute of Oxygen Supply, Tibet University, Lhasa, 850000, PR China

## ARTICLE INFO

### Keywords:

Ni/NiO@polyaniline  
Bifunctional catalyst  
4-Nitrophenol  
Epinephrine  
Nanomolar detection.

## ABSTRACT

It is extremely significant to address an urgency toward the development of low-cost and efficient catalysts. Herein, for the first time, we synthesize a novel self-assembled Ni/NiO@PANI by a combustible crystallization followed polymerization method, constructed by impregnation of Ni/NiO in sulfonic acid-doped polyaniline, which can be used as a bifunctional catalyst for electrochemical sensing of epinephrine (EP) and reduction of nitro- to amino-phenol (4-NP to 4-AP). Due to the unique nanoarchitecture, ferromagnetic feature of Ni, anti-corrosion feature of PANI, and synergy between the system (metal/metaloxide@carbon) leads superior performance: it can rapidly reduce the 4-NP pollutant to environmentally friendly 4-AP within 8 min, and easy magnetic recycling; Also, it can be used as a sensor for EP neurotransmitters with a sensitivity, detection, and quantification limit of 0.117 nA $\mu\text{M}^{-1}$ , 87.2, and 290.71  $\mu\text{M}$ , respectively. This work provides a strategy to design low-cost and superior catalysts applied in catalysis and electrochemical sensor.

## 1. Introduction

In general, noble metals (Au, Ag, and Pt) are being demonstrated as one of the outstanding catalysts in various organic transformations and sensing applications. However, they are highly expensive and every so often suffers from a sudden fall in catalytic activity due to the aggregation and leach of particles, which cause limits in large-scale applications [1–3]. Hence, more attention to constructing excellent earth abundant or non-noble metal-based catalysts is required. Especially, non-noble metal-based multicomponent hybrid systems also drawn wide attention among scientists owing to its inexpensive, earth-abundant, low toxic, adsorptive nature, magnetic-center, lattice order/disorder behaviours, fast ion/charge diffusivities, intrinsic corrosion resistance, high surface area, and good conductivity [4,5]. However, the progress of low-cost, recoverable, and highly efficient bifunctional catalysts for pollutant reduction and detection using earth-abundant materials has

endured as the big-challenge due to its sluggish electrochemical kinetics, poor structural stability, and low electrical conductivity. To improve the existing properties of earth-abundant catalysts, doping [6,7], surface functionalization [8], and composite/hybrids [9] are reported with considerable attention. Among these, the fabrications of semiconductor/carbon catalysts with core-shell nanoarchitectured hybrids have extensive attention and more favorable towards potential applications including, memory devices, sensors, electrochromic films, cathode in a battery, catalysis, and magnetic materials [10–16]. For instance, it is often demonstrated that the existence of carbon support with transition-metal oxides could provide them superior d-band electronic DOS (density-of-states) at the Fermi level, which boosts physicochemical features [17–19]. Specially, the addition of acid-doped conducting polymers (polyaniline) or heteroatom-doped graphene oxide is significantly enhanced the electrochemical sensing behaviour of semiconductor materials [20,21]. Hence, we intended to synthesis

\* Corresponding author at: School of Electronic Science and Engineering and State Key Laboratory of Electronic Thin Films and Integrated Devices, University of Electronic Science and Technology of China, Chengdu, 610054, PR China.

\*\* Corresponding author.

E-mail addresses: [yfchen@uestc.edu.cn](mailto:yfchen@uestc.edu.cn) (Y. Chen), [vnnara@yahoo.co.in](mailto:vnnara@yahoo.co.in) (N. Vengidusamy).

<https://doi.org/10.1016/j.apcata.2021.118028>

Received 23 November 2020; Received in revised form 28 January 2021; Accepted 31 January 2021

Available online 8 February 2021

0926-860X/© 2021 Elsevier B.V. All rights reserved.

ultra-small Ni/NiO nanoparticles embedded within conducting polyaniline (DBSA-PANI) to attain core-shell nanoarchitected hybrids for fast electron-transfer ability with maximal current density.

In general, all the nitro-aromatics are known to be certainly poisonous than amino-aromatic compounds. As an utmost refractory pollutant, 4-NP is regularly coexistent in industrial effluents, whereas its reduced compound (4-AP) is utilized as a photo developer, anticorrosion-lubricant, hair-dyeing compound, analgesic, and antipyretic drugs [22]. Hence, the catalytic chemical conversion of 4-NP hazards into environment-friendly 4-AP is crucial. Likewise, epinephrine (EP) is another important neurotransmitter complicated in dynamic biological processes, in which the detection of EP at physiological conditions is a crucial requirement. EP is commonly known as adrenaline and this one stimulates glucose production in the biological systems and changes in the concentration or abnormal levels of EP inside the digestive scheme leads to neurological disorders and quite a lot of illnesses including in a digestive, mood/sleep, emesis, sexuality, and appetite [23–25]. Also, epinephrine is an electrochemically active compound and its electro-kinetics has been measured widely. Hence, the catalytic chemical conversion of 4-NP hazards into environment-friendly 4-AP and detection of EP in clinic medicine at practical conditions is a crucial requirement. A key challenge in a fabrication of metal/oxide/carbon core-shell hybrids/composite materials is particle size and homogenous distribution, which requires multi-step profound complex procedures. Herein, among several possible fabrication pathways, we chose a relatively facile combustible redox crystallization reaction and subsequent oxidative polymerization technique for Ni/NiO@PANI hybrids synthesis with uniform size distribution; besides, embedding within polymer may arrest the post oxidation of nickel, thus advances the physicochemical properties and excellent stability of as-synthesised catalysts. Herein, for the first time, by using a combustible crystallization followed by the oxidative polymerization method, a novel sulfonic acid-rich PANI covered Ni/NiO core-shell nanohybrid is synthesized for the catalytic conversion of 4-NP and electrocatalytic detection of EP. The most intriguing feature could be microstructure and homogeneity in Ni/NiO@PANI core-shell structure and the synergy arises between acid-base sites, which boosts the catalytic performances. Due to its unique core-shell nanoarchitecture, the ferromagnetic feature of Ni, and the anti-corrosion feature of PANI, the Ni/NiO@PANI catalyst show superior performance. The physicochemical properties of Ni/NiO@PANI, the catalytic reduction of nitro- to aminophenol, and electrocatalytic detection of EP have been systematically investigated.

## 2. Experimental section

### 2.1. Materials and agents

Nickel (II) acetate, aniline ( $C_6H_7N$ ), ammonium carbonate ( $CH_8N_2O_3$ ), ethylene glycol (EG,  $C_2H_6O_2$ ), hydrazine ( $N_2H_4$ ), 4-nitrophenol (4-NP), dodecylbenzene sulfonic acid (DBSA,  $C_{18}H_{30}O_3S$ ) and borohydride ( $NaBH_4$ ) were bought from SRL India Ltd. Epinephrine (EP) was purchased from Sigma-Aldrich. For the making of buffer (pH (1–9)), sodium dihydrogen phosphate ( $NaH_2PO_4$ ), disodium hydrogen phosphate ( $Na_2HPO_4$ ), sodium acetate ( $C_2H_3NaO_2$ ), acetic acid ( $C_2H_4O_2$ ), hydrochloric acid (HCl), sodium hydroxide (NaOH), potassium chloride (KCl), and ethanol were used (Merck) and deionized (DI) water was used as a solvent for all the experiments. Before the preparation of polyaniline (PANI), aniline was freshly distilled.

### 2.2. Ni/NiO nanomaterial

The Ni/NiO nanomaterial was prepared by a facile combustible redox crystallization strategy. Briefly, the aqueous 0.01 M  $Ni^{2+}$  and 10 % ethylene glycol solutions were gradually added into 1 mM hydrazine: 0.01 M ammonium carbonate. The initial colour of the pale-green

solution was turned to purple and then bluish during the slow addition of hydrazinocarbonic acid mixture (aqueous 0.01 M ammonium carbonate mixture and 1 mM hydrazine ( $N_2H_4$ ) with 1:0.1 ratio). These intermediate precursors were stirred for half an hour at 60 °C in a magnetic stirrer and then centrifuged. Excessive addition of  $N_2H_4$  in hydrazinocarbonic acid mixture might result in a dark blue solution, due to the excessive solubility of an intermediate precursor. Finally, the precipitates were washed well with the water-ethanolic mixture, and the resulting powders were combusted and kept in a muffle furnace in an air atmosphere at 300 °C for 30 min to increase the polycrystalline nature of Ni/NiO. The same precipitates are treated at 500 °C for 2 h in an air atmosphere and argon atmosphere at 300 °C for 90 min to obtain NiO and  $Ni^0$  samples, respectively.

**Caution:** The obtained precipitates are found to be explosive and too vigorous with nickel nitrate in its place of nickel acetate.

### 2.3. Synthesis of the Ni/NiO@PANI nanohybrid

The Ni/NiO@PANI, NiO@PANI, and DBSA-PANI nanohybrids were synthesized by a self-assembled oxidative polymerization method in presence of DBSA. The experimental procedure is given as follows: 0.02 mL of aniline monomer was mixed with the solution of DBSA, dissolved in 150 mL DD water to form an emulsion of aniline-DBSA complex. The reaction is maintained at 5 °C under stirring for 45 min. Then aqueous ammonium persulphate (APS) as an oxidant to the above reaction mixture was mixed well before the addition of the quantitative amount of Ni, NiO, or Ni/NiO nanoparticles (0.2 g) in aniline-DBSA/APS (the ratio of aniline, DBSA, and APS is 1:0.2:2 w/w), which was left overnight to obtain blackish-green colloids of Ni@PANI, NiO@PANI or Ni/NiO@PANI nanohybrids, respectively. The products were washed with DI water three to five times and then dried under a vacuum for a day. The same synthetic procedure was followed to obtain DBSA-PANI (the ratio of aniline, DBSA, and APS is 1:0.2:2 w/w) in the absence of NiO and Ni/NiO.

### 2.4. Characterization techniques

The crystalline and structural data of the nanohybrids were determined with Rich-Siefert 3000 diffractometer - Cu  $K_{\alpha 1}$  ( $\lambda = 1.5406 \text{ \AA}$ ) radiation. HR-XPS measurements were done using GMBH, Omicron nanotechnology, 1483 eV monochromatic Al  $K_{\alpha}$  (XM-1000) source, Germany, operated at 0.3 kW, 15 kV, emission current-20 mA, and a 50 nbar base pressure. The survey measurements were accomplished with a step size - 0.5 eV along with pass energy - 50 eV. The high-resolution emission scans were made with 30 meV as the step size and pass energy - 20 eV with 3 sweep segments. The DRS-UV-vis absorbance was recorded by the Perkin-Elmer spectrophotometer and FTIR spectra were recorded with the Perkin-Elmer Infrared spectrometer. Magnetic spectra were executed at RT using a Lakeshore-7404 vibrating-sample-magnetometer. The morphologies of DBSA-PANI, Ni/NiO, and Ni/NiO@PANI nanohybrids were analyzed by FE-SEM, HITACHI SU6600 field emission EDAX coupled SEM, and TEM, FEI TECNAI using T-30, G2 model with 200 kV accelerating voltage.

### 2.5. Electrochemical sensing of epinephrine (EP)

The electrochemical sensing measurements were implemented at RT using a CHI1103A three-electrode cell electrochemical-workstation, in which a sat. A calomel electrode (SCE) was a reference, a platinum electrode was a counter and a glassy-carbon electrode (GCE) was a working electrode throughout the experiments. The CV's were achieved at a fixed potential window (various scan rates of .01 to 0.5  $Vs^{-1}$ ) in  $N_2$  saturated 0.1 M buffer solutions. Our previous drop-cast assisted electrode fabrication methods were used for the catalyst loading process on the electrode. Briefly, the ultrasonicated catalyst suspensions were made by dispersing 2 mg of electrocatalysts in 1.5 mL of ethanol and 0.5 mL

water. From this ultrasonicated catalyst suspension, 5  $\mu\text{L}$  was dropped on the surface of highly-polished GCE and dried in an oven. Various  $\text{N}_2$  saturated pH (1–9) solutions were adjusted with the aid of pH meter using the below-prepared stock solutions, 0.1 M KCl and HCl for pH (1–2 buffered-saline), 0.1 M  $\text{CH}_3\text{COOH}$ ,  $\text{CH}_3\text{COONa}$  (ABS, pH 3–5 acetic acid buffered-saline), and 0.1 M  $\text{Na}_2\text{HPO}_4$ ,  $\text{NaH}_2\text{PO}_4$ , and 0.1 M NaOH (PBS, phosphate-buffered saline pH > 6) into 1 L of DI water.

## 2.6. Catalytic conversion of 4-NP

An aqueous dispersion of ultrasonicated catalyst (10 mL containing 4 mg) was added with aqueous 0.3 M  $\text{NaBH}_4$ , then the suspensions were stirred for a few minutes at RT. 4-nitrophenol (3 mM) was mixed to the suspensions, which was agitated until a bright-yellow solution colour progressively turn to colourless (Figs. S1, S2). The reduction reaction progress had been monitored with a UV–vis absorption spectrophotometer.

## 3. Results and discussions

### 3.1. Structural studies

The diffraction patterns recorded for PANI, NiO@PANI, and Ni/NiO@PANI are shown in Fig. 1a. NiO@PANI exhibits diffraction peaks at  $37.3^\circ$ ,  $43.3^\circ$ , and  $62.9^\circ$  corresponds to (111), (200), and (220) planes, respectively of cubic NiO (JCPDS No. 065-5745). The Ni/NiO@PANI shows additional diffraction peaks at  $44.7^\circ$  and  $51.8^\circ$  due to (111), and (200) crystal planes, respectively of cubic structured  $\text{Ni}^0$  (JCPDS No; 065-0380) along with peaks of NiO. In the PXRD patterns of PANI, NiO@PANI, and Ni/NiO@PANI, broad diffraction peaks ( $20\text{--}30^\circ$ ) has risen due to parallel polymer chain, but diffraction peaks correspond to the polymer at Ni/NiO@PANI are less clearly observed [26]. This may be due to the dominant polycrystalline Ni/NiO diffraction peaks. However, the diffraction peak intensities of Ni/NiO@PANI are look suppressed could be due to the shell-like formation of the PANI layer on the core inorganic particles.

Fig. 1b shows the FTIR spectra of PANI, NiO@PANI, and Ni/NiO@PANI composite structures. The FT-IR spectrum of hybrid shows characteristic bands as shown in Fig. 1b corresponds to DBSA-doped PANI. In particular, the band recognized at  $\approx 1320\text{ cm}^{-1}$ , and the band at  $\approx 1580\text{ cm}^{-1}$  attribute to the presence of benzenoid-quinoid (aromatic Q–B) rings (stretching C=N, and CC= vibrations), and the peak at  $\approx 1265\text{ cm}^{-1}$  is recognized associated to the emeraldine state bipolaron polymer structure [26,27]. Additionally, high-intensity peaks between  $\approx 1005\text{--}1150\text{ cm}^{-1}$  are closely related to the respective symmetric sulphonic (S–O)/asymmetric SO= stretch vibrations, which clearly confirm the presence of sulphonic acid-rich polyaniline [2,28]. In addition, The FTIR spectrum of Ni/NiO@PANI shows broad peaks at 3380, and 2980–2870/870  $\text{cm}^{-1}$  agree with NH– stretching mode, and

aliphatic C–H stretching/bending modes, respectively [2,26]. The peaks owing to PANI are clearly described, but the peak corresponds to  $\nu_{\text{Ni-O}}$  stretching vibration of NiO are less clear (Fig. S2), in contrast, the presence of Ni/NiO into a Ni/NiO@PANI is well-identified through XRD studies. Following this, the FT-IR bands of NiO@PANI and Ni/NiO@PANI composites are almost similar with significant peak suppression with a slight change in peak position. Hence these corresponding data confirm the formation of Ni/NiO impregnated sulphonic acid-rich polyaniline nanocomposites, which are in good-agreement with PXRD, and XPS (Figs. 1 and 2).

The XPS survey spectrum of Ni/NiO@PANI composite nanostructures (Fig. 2a) shows that the composite is composed of Ni, C, N, O, and S elements merely. It can be noted that the Ni/NiO@PANI (Fig. 2b) shows multiple split peaks (Ni  $2p_{3/2}$ ) at 853.1, 855.3, and 860.4 eV, which corresponds to a metallic  $\text{Ni}^0$ , oxidized form of Ni-O and shakeup satellite peaks [29]. The deconvoluted Ni  $2p_{3/2}$  core level emission peak is centered at about 855.3 eV with corresponding superimposed multiple splits, Ni  $2p_{1/2}$  at about 873.1 eV, and a spin-energy separation of  $\Delta E = 17.8\text{ eV}$ , as shown in Fig. 2b. The XPS core level spectrum of the O 1s (Fig. 2c) shows a peak at 528.6 V related to adsorbed oxygen ( $\text{O}_2$ ), 530.35 eV related to the NiO lattice oxygen (Ni-O), while a broad peak is observed at 532.6 eV can be associated to a surface hydroxyl group (–O–H) [30]. The deconvoluted C 1s core-level spectrum shows three peaks (Fig. 2d). The peak at 284.6 eV is related to the C–C, the peak at 285.9 eV is related to the CN– group and the peak at 287.6 eV can be recognized as the O–CO= group [29,31]. The deconvoluted XPS core level spectrum of N 1s exhibits 3 peaks (Fig. 2e). The peak, 399.3 eV is associated with amine (–N=) and a 401.9 eV peak is associated with  $\text{N}^{*+}$  (both polarons and bipolarons) at the binding energy range of N1 s. The 403.8 eV peak is related to the protonated amine, which is observed at higher binding energy because of the strong electron localization associated with  $sp^3$  bonded poor-conjugated sites. The high-resolution XPS spectra of the  $\text{SO}_4^{2-}$  core level peak is centered at about 169.65 eV (Fig. 2f), which is observed due to the associated DBSA within the PANI composite [32].

### 3.2. The formation mechanism of Ni/NiO@PANI composite nanostructures

The FE-SEM and TEM images are presented in Fig. 3a, b and c, d, respectively correspond to PANI (Fig. 3a, c) and Ni/NiO@PANI (Fig. 3b, d) nanostructures. It can be established that the three-dimensional structures are constructed with tube-shaped polymers with inorganic particles. The homogenous distribution of a particle tells a possibility of extraordinary interaction occurs between Ni/NiO particles and PANI. Similarly, the FE-SEM and TEM images of Ni/NiO nanostructures are shown in Figs. S3a and S3b-c, respectively. The FESEM image, EDAX elemental analysis, and composition of as-synthesized PANI and NiO@PANI are shown in Fig. S4 and S5, which confirm the presence of

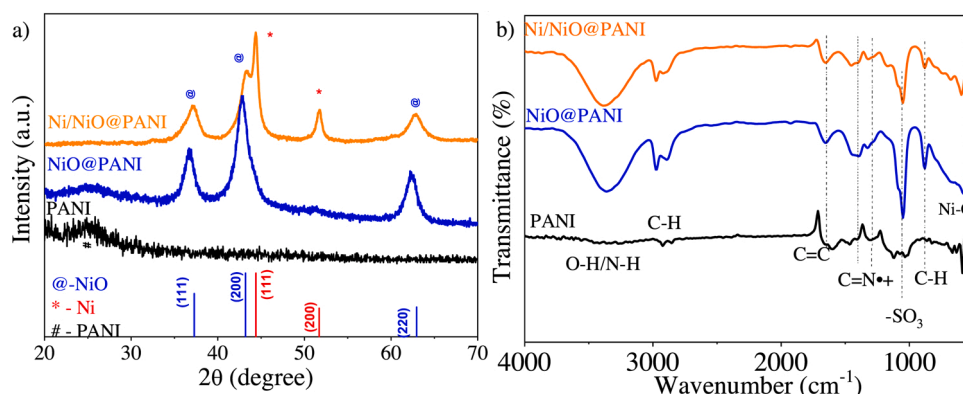


Fig. 1. a) XRD patterns and b) FTIR spectra of PANI, NiO@PANI, and Ni/NiO@PANI.

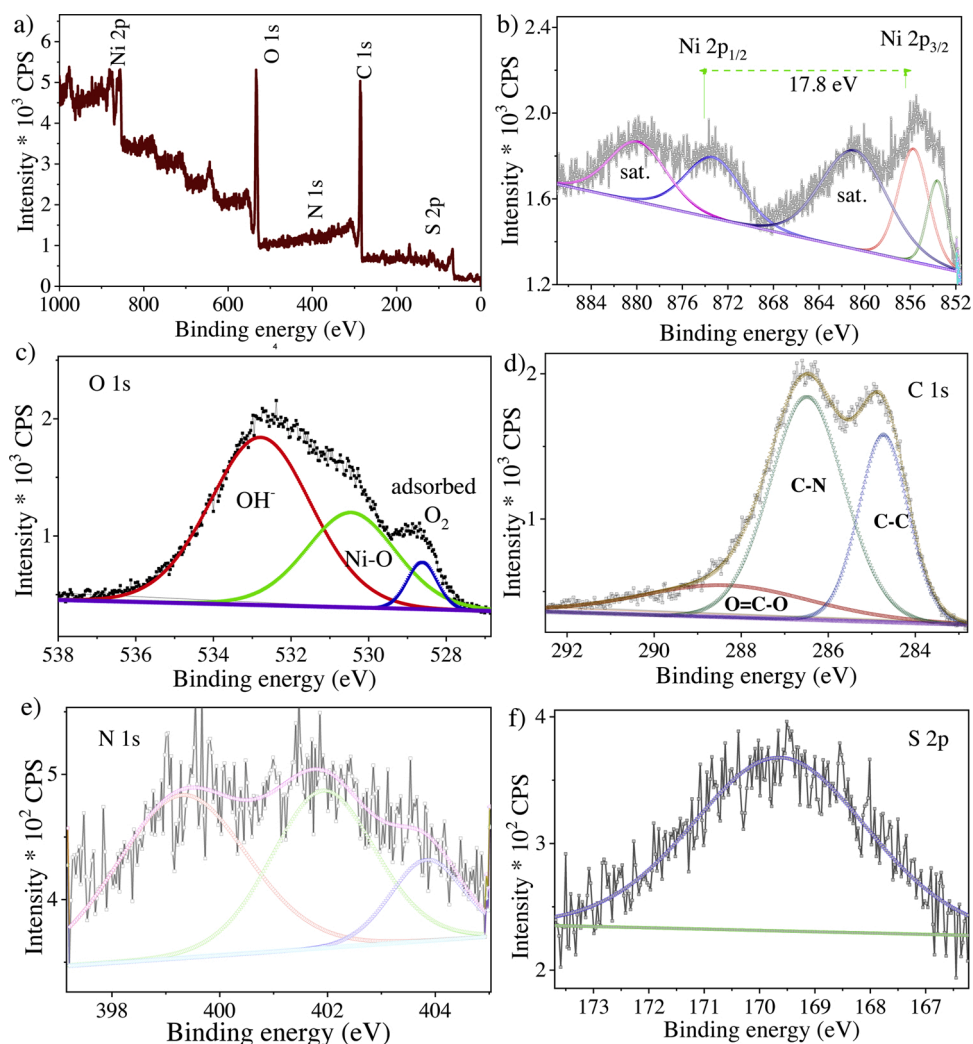


Fig. 2. (a) XPS survey spectrum, (b-f) Ni 2p, O 1s, C 1s, N 1s, and S 2p core-level spectra of Ni/NiO@PANI, respectively.

N, C, S, Ni, O, and the existing elements quantitative weight percentages, respectively. These obtained results are in good agreement with FTIR (Fig. 1b), and XPS (Fig. 2) studies, which clearly confirm the formation of hierarchical sulphonic acid-rich polyaniline nanostructures.

We can see the carbon tubes are decorated with spherical particles. It confirms that the Ni/NiO attached to the surface of the PANI layer nanoparticles, and the PANI layer is relatively thicker. As per attained results and discussion, the formation of Ni/NiO@PANI composite nanostructures can be explained as follows: initially, based on reports [23,26], the possible formation of Ni/NiO (combustible redox synthesized) could be explained through the thermal growth of N-N-rich high-energy nickel hydrazinocarboxylate precursor, which is explosive at high temperature; secondly, Ni/NiO core and PANI outer shell are designed as Fig. S3. In brief, when the DBSA/ANI/APS is added into the dispersion containing Ni/NiO nanoparticles, the dodecyl benzene sulphonates are adsorbed uniformly on the surface of the nanoparticles. Moreover, the aniline monomer is reacted in the above DBSA solution, which becomes protonated anilinium cation ( $\text{ANI}^+$ ), thus uniformly adsorbed on a Ni/NiO nanoparticles ( $\text{Ni/NiO-DBSA}^{\delta-}\text{-ANI}^{\delta+}$ ) owing to prevalent electrostatic attraction. Herein, the reaction of ammonium persulphate (APS) as a strong oxidant (Ni/NiO-DBSA-ANI/APS), the polymerization is initiated, which outcomes the conductive sulfonic acid-rich polymer layer on the Ni/NiO particles thus results in Ni/NiO@PANI nanostructures. Following this, the combustible redox crystallized followed by oxidative polymerization mechanism (self-assembly solution-solid-solid growth) is proposed based on our

experimental results detailed above.

### 3.3. Physicochemical behaviours of Ni/NiO@PANI

The UV-vis absorption spectra of NiO@PANI, and Ni/NiO@PANI nanostructures are shown in Fig. 4a. The absorption spectrum shows two absorption bands at approx. 390 and 690 nm can be assigned to carbon support (PANI) and (Ni—O), respectively [23,27,33]. The absorption band approx. 390 nm corresponds to  $\pi\text{-}\pi^*$  transition and band at approx. 550–750 nm corresponds to benzenoid rings into quinoid ring transitions [32]. The absorption spectrum of Ni/NiO@PANI compared to that of NiO@PANI shows that the corresponding peak positions of benzenoid-quinoid ring transition are shifted to lower wavelengths. The NiO@PANI and Ni/NiO@PANI composites result in narrowed transitions with wavelength shift, where the electron transitions become easier, thus suppresses the energy gap [34]. The absorption band of Ni/NiO@PANI composite nanostructures resembles the NiO@PANI absorption band. The bandgap,  $E_g$  is calculated from Tauc's (Tauc's equation:  $\alpha h\nu = A(h\nu - E_g)^2$ ) plot. The value of  $h\nu$  extrapolated to zero absorbance ( $\alpha = 0$ ) gives the direct allowed transition (bandgap) between valence to conduction band excitation. The order of  $E_g$  value is NiO@PANI > Ni//NiO@PANI, as shown in Fig. 4b. The synthesized Ni//NiO@PANI results in a spectral shift to its nanoscale particles of Ni//NiO corresponds to its quantum confinement effect.

The M-H curves of NiO@PANI and Ni/NiO@PANI measured at 298 K are shown in Fig. 4c. As shown in Fig. 4d, the Ni/NiO@PANI

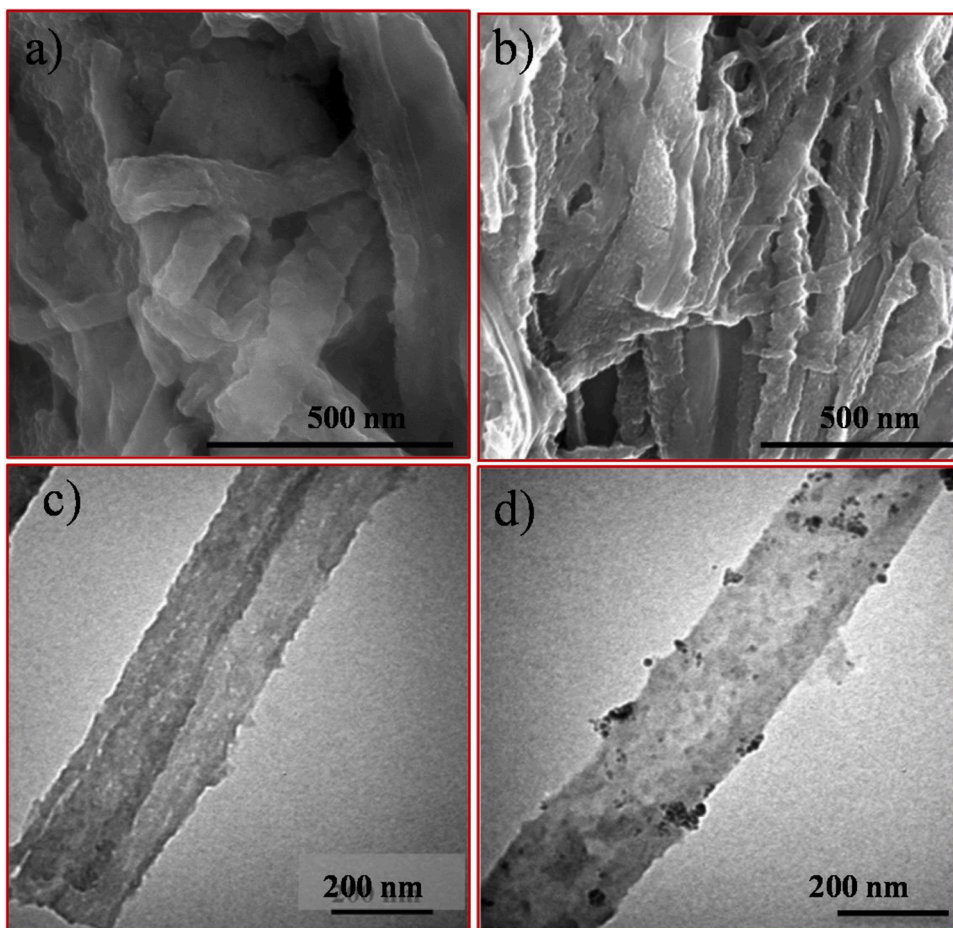


Fig. 3. a, b) SEM and c, d) TEM images of PANI, Ni/NiO@PANI, respectively.

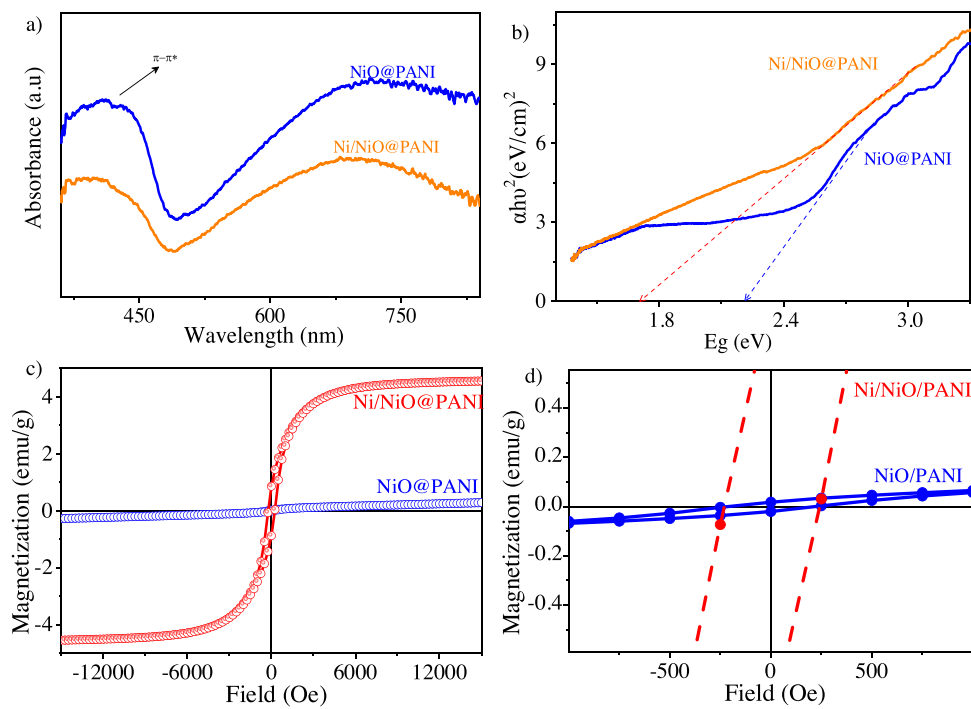


Fig. 4. a) DRS UV-vis absorption spectra b) Tauc's plot, c) M-H curves and d) magnified illustration of NiO@PANI and Ni/NiO@PANI.

composite shows a ferromagnetic behavior due to the presence of magnetic Ni metal sites along with NiO. However, the NiO@PANI shows more or less a paramagnetic behavior, which is mainly contributed by the coreless NiO and PANI. The cyclic voltammogram of Ni/NiO@PANI in 0.1 M H<sub>2</sub>SO<sub>4</sub> is presented in Fig. 5a. The voltammograms are characterized by three anodic and corresponding three cathodic peaks, indicating electroactive regions with three well-defined redox electrochemical systems [35]. The initial redox-reaction (first redox peak at approx. 0.49 V) is associated with the transition between fully-reduced leucoemeraldine-semiconductor results in half-oxidized emeraldine-conductor, whereas the second redox peak at approx. 0.38 V is associated with oxidized products free in the polymeric-matrix. A third transition peaks at approx. 0.09 V indicates the redox reaction of emeraldine-*pernigraniline* species as an oxidized form of PANI. EIS spectra circuit fit endorses the higher charge/ion transport behaviour of Ni/NiO@PANI/GCE compared to bare GCE, as shown in Fig. 5b.

The pH effect on a voltammogram of Ni/NiO@PANI is studied between pH 1–9. As seen in Fig. 5c, the respective peak potentials of the redox couple are shifted more negatively with respect to increasing pH, which is triggered by the initial protonation of a sulfonic group functionalized amines in a polymer chain. These charge transfer redox couples are not detected at pH values higher than pH 6.0. The following conclusions (the lack of electrochemical activity and being of electrochemical behaviour can be found at more-negative potential while moving toward basicity) may be incidental based on behaviour of PANI peak couple at higher pH solutions. The CV's of sulfonic acid-rich PANI in 0.1 M H<sub>2</sub>SO<sub>4</sub> at various scan rates (10–500 mV/s) are displayed in Fig. 5d. As expected, it can be seen that the respective peak potentials and its corresponding current values are varied with a change in scan rates. These results indicate that the synthesized PANI nanotubes are electroactive and the charge/ion transfer process is coupled to the diffusion processes, to be precise, the hopping assisted electron transportations are along the sulfonic group functionalized conjugated polymeric nanostructures.

### 3.4. Catalytic reduction of 4-NP to 4-AP transformation

To evaluate the excellence of Ni/NiO@PANI catalyst, the potential catalytic reduction reaction of 4-Nitrophenol (4-NP) is confirmed. The UV–vis absorption spectra of the 4-NP reduction reaction are displayed in Fig. 6. The schematic catalytic reaction of 4-NP reduction is explained in Fig. S2 and the proposed mechanistic paths are almost similar to previous mechanisms [36]. In general, 4-NP favorably interacts with the metal surface in the presence of excess NaBH<sub>4</sub> and undergoes a reduction of nitro groups. Here, NiO, Ni, and Ni/NiO along with polymer-supported materials are used as the catalyst for 4-NP reduction. Catalytic reduction of 4-NP starts with color intensification as yellow to dark yellowish, in a presence of catalyst and NaBH<sub>4</sub>, which notifies a formation of an intermediate system (4-nitrophenolate-BH<sub>4</sub>) as shown in Fig. 6a. As evidenced, in presence of Ni/NiO@PANI, while reacted with an aqueous NaBH<sub>4</sub>, an absorption band (~400 nm) associated with 4-nitrophenolate-BH<sub>4</sub>, the system is decreased with the increase in absorbance at 298 nm (Fig. 6b), which infers that desorption of 4-AP as a reaction product from a catalyst surface [20,36]. In accordance with the results, the adsorption-desorption followed catalytic reduction reaction proceeds rapidly with the time of about 8 min as presented in Fig. 6c. Besides, the Ni/NiO@PANI facilitates outstanding catalytic performance than the other obtained catalysts (PANI, Ni@PANI, and NiO@PANI). The kinetic plot ( $\ln(A_t/A_0) = -kt$ , where  $k$  - constant,  $A_t$  - relative absorption intensity and  $t$  - time) of 4-NP reduction has showed the pseudo-first-order reaction kinetics with an order of  $k$  value: PANI (0.002 s<sup>-1</sup>) NiO@PANI (0.024 s<sup>-1</sup>) < Ni@PANI (0.236 s<sup>-1</sup>) < Ni/NiO@PANI (0.31 s<sup>-1</sup>), as displayed in Fig. 6d. The greater  $k$  value suggests the excellent catalytic activity of materials, which suggests the significant role of Ni particles at NiO@PANI towards the 4-NP reduction, and also these results are comparable with reports. The observed excellent catalytic reduction efficiency (Fig. 6e) is owing to its synergetic/interfacial-coupling effect between Ni/NiO particles and PANI backbone. More interestingly, the change in color (yellowish to colorless) has been noticed due to the conversion of 4-nitrophenol to its

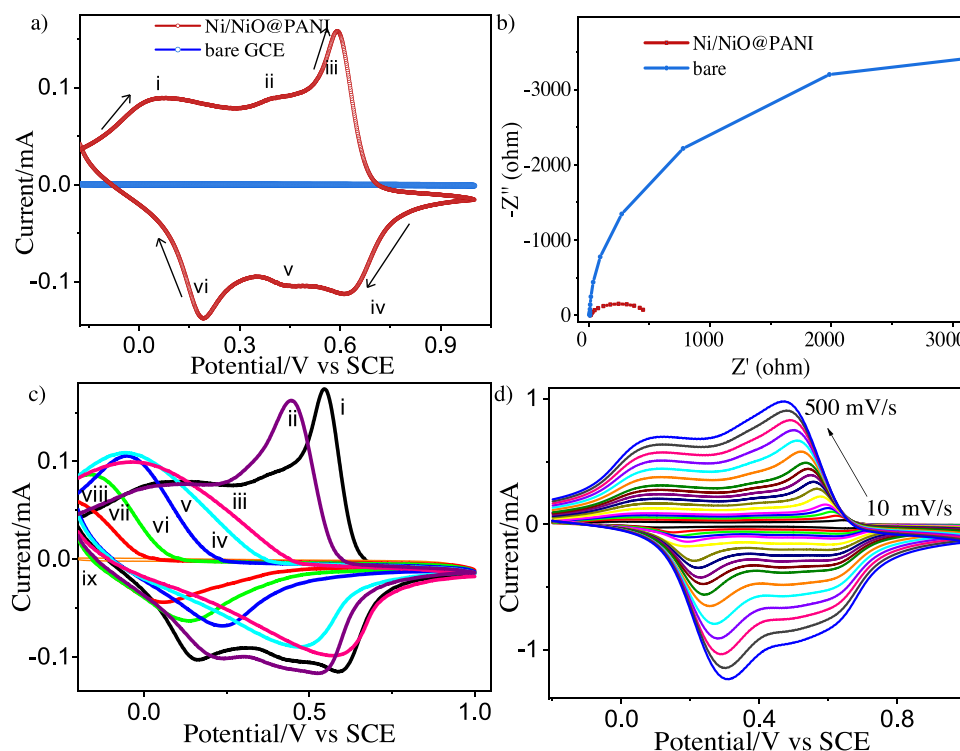


**Fig. 5.** a) CV and b) EIS of bare and Ni/NiO@PANI. c) Effect of pH (1-9) on peak potentials and peak currents. d) Cyclic voltammograms of Ni/NiO@PANI in 0.1 M H<sub>2</sub>SO<sub>4</sub> at various scan rates.

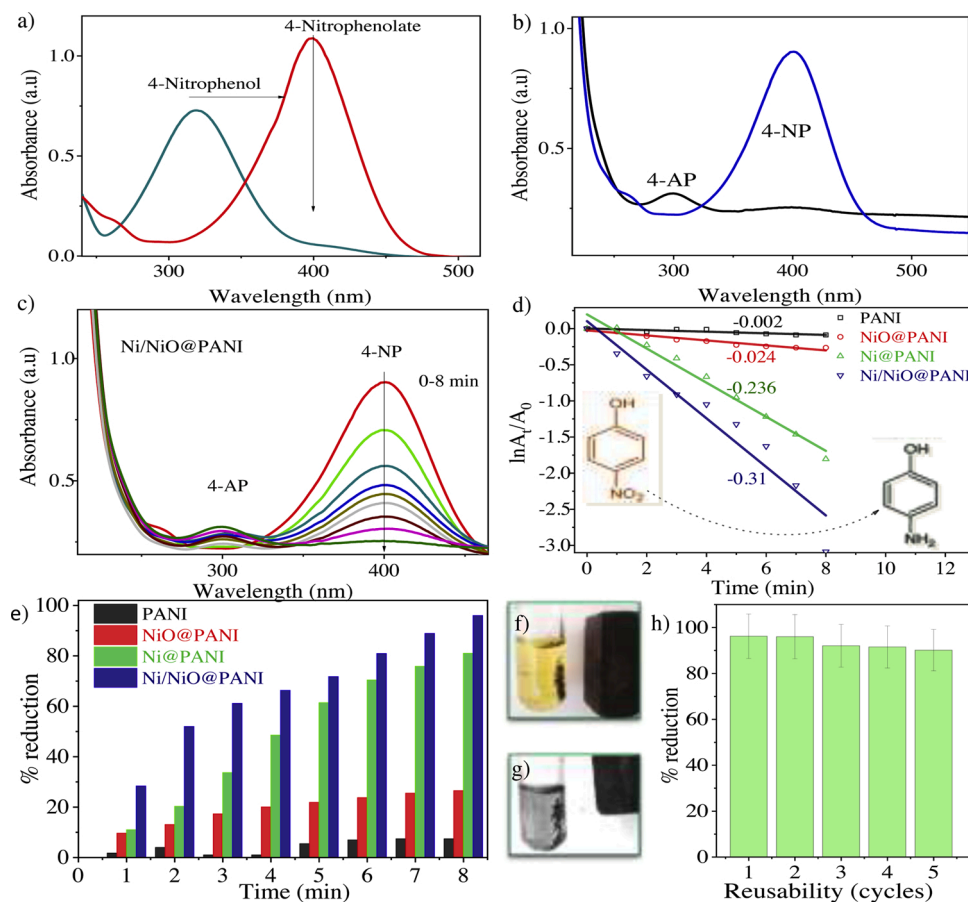


**Fig. 6.** a-c) Time-dependent UV-vis absorption spectra of before, during, and after the 4-NP to 4-AP catalytic reduction, d)  $\ln(A_t/A_0)$  versus time kinetic plot, e) reduction efficiency, f) before catalysis g) after catalysis and h) catalytic reusability test of 4-NP reduction.

corresponding aminophenol as observed in Fig. 6f, g. After catalysis, the magnetic recovery highlights the advantages of Ni/NiO@PANI to determine the catalytic reusability and long-term behaviors. The magnetically recovered catalysts are washed well using water followed by acetone, while applied for reusability test; the catalyst is performing excellent until five cycles as shown in Fig. 6h. Herein, excellent long-term reusability of Ni/NiO@PANI could be achieved by a PANI surface, which prevents the surface fouling and agglomeration of Ni/NiO particles (the catalytic centers for reduction reaction).

### 3.5. Electrocatalytic sensing of epinephrine

Fig. 7 depicts the CVs of  $1 \times 10^{-4}$  M EP (0.1 M acetate buffer saline, ABS, pH = 5) at bare GCE, NiO@PANI/GCE, and Ni/NiO@PANI/GCE with a scan rate of  $50 \text{ mVs}^{-1}$ . Ni/NiO@PANI/GCE represents well-defined redox peaks correspond to the dissolved neurotransmitter (EP) with the maximal current than NiO@PANI/GCE, while bare GCE (Fig. 7) shows negligible current with a broad oxidation peak current. Based on the above discussion and the previous report [37–39], the electrocatalytic redox mechanism of EP at Ni/NiO@PANI can be explained as shown in Fig. 7.

Figs. 8a, and S6a show an influence of the scan rate on an

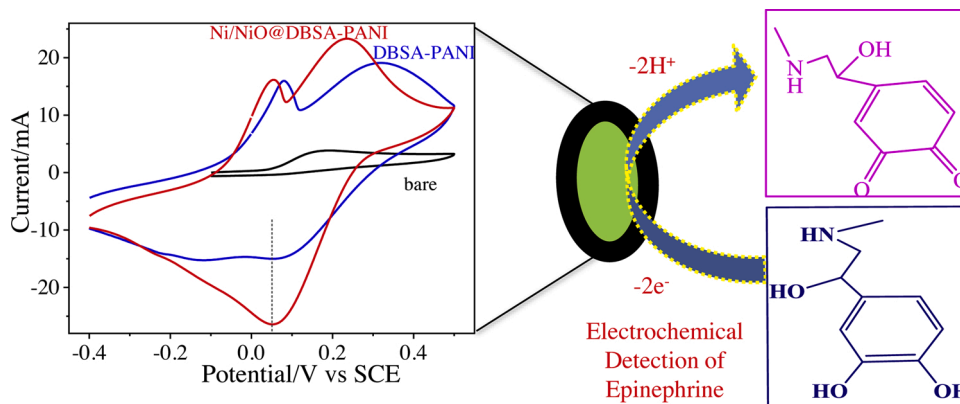


**Fig. 7.** CVs of  $1 \times 10^{-4}$  M EP in 0.1 M ABS at  $50 \text{ mVs}^{-1}$  and pictorial view of redox behaviour of EP at Ni/NiO@PANI/GCE.

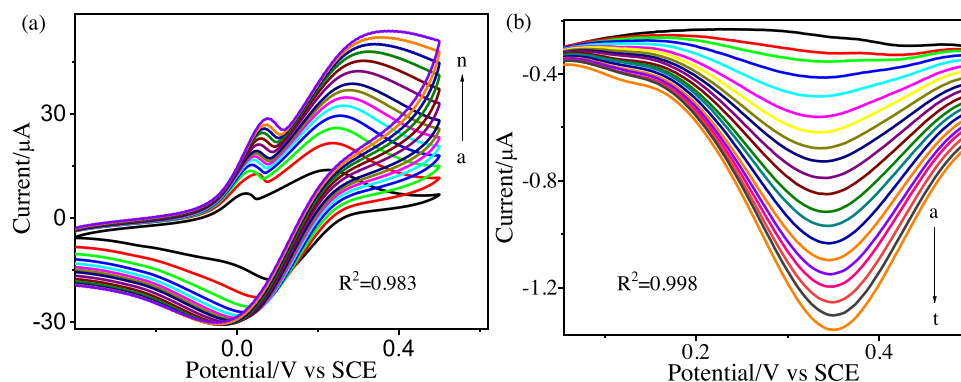


Fig. 8. a) CVs with different scan rates and b) DPVs with different concentrations vs. current of EP at Ni/NiO@PANI/GCE.

electrocatalytic response of  $0.1 \times 10^{-3}$  M EP at Ni/NiO@PANI, with various scan rates of a) 25, b) 50, c) 75, d) 100, e) 125, f) 150, g) 175, h) 200, i) 250, j) 300, k) 350, l) 400, m) 450, and n) 500 mV/s, respectively in 0.1 M ABS solutions. The peak current corresponds to anodic oxidation potential is moved positively and cathodic reduction is moved negatively. Figs. 8a and S6 demonstrate that the peak currents are linearly proportional to a square root value of the scan rates ( $\nu^{1/2}$ ) between 25–500 mV s<sup>-1</sup>. Collectively, all these results recommend that the Ni/NiO@PANI electrocatalyst has efficient electrocatalytic and fast charge transfer activity towards the detection of EP and these findings are consistent with the reports [40–45]. Likewise, it is also suggesting that the electrode processes relate to a diffusion-controlled reaction (Fig. S6a). The number of charge transfer involved in these processes can be obtained by this equation: Number of electrons =  $4IRT/Q\nu$ , accordingly, the total number of e- transfer involved in this EP redox process is 2, whereas,  $I_p$  is a peak current,  $R$  is a gas constant,  $Q$  is a charge,  $F$  is a Faraday, and  $\nu$  is scan rate).

The linear regression equation for an EP redox process:  $I_a = 1.121 \nu^{1/2}$  (mVs<sup>-1</sup>)<sup>1/2</sup> - 3.720 ( $R^2 = 0.983$ ) (Fig. S6a).

The linear equation:  $I(\mu A) = 0.0117 [EP] (\mu M) + 0.2533$  ( $R^2 = 0.9987$ ) (Fig. S6b).

Fig. 8b displays the DPV plot of current concerning the EP concentration at Ni/NiO@PANI/GCE in 0.1 M ABS. The peak current corresponds to the EP in between the range of 0 to 0.6 V potential windows are increased gradually with an EP gradual addition. The calibration plot for the determination of EP is plotted as shown in Fig. S6b, the linear range is found between  $1-100 \times 10^{-6}$  M with nanomolar sensitivity of  $0.117 \text{ nA } \mu\text{M}^{-1}$ . The obtained detection limit and quantification limit values are 0.087 nM and 0.29 nM, respectively. The results suggest that the Ni/NiO@PANI electrocatalyst on GCE possesses an ultrahigh nanomolar sensitivity towards oxidation of EP. Overall, the significant shift in the overall anodic oxidation and cathodic reduction peaks of Ni/NiO@PANI/GCE than NiO@PANI/GCE, toward the less positive region with respect to  $1 \times 10^{-4}$  M epinephrine, might be attributed to its multi-component synergetic/coupling effect between semiconductor (Ni/NiO) and conductive carbon (PANI). This electrocatalytic sensing property is mainly attributed to the available abundant Ni/NiO electro-active catalytic sites within PANI composite nanostructures. Finally, to check the stability of Ni/NiO@PANI/GCE, the electrode is stored for a month at 5 °C at after the detection test, since the current only reduced by approx. 5 %, which could be attributed to the excellent protection effect of PANI against the desorption or decomposition of Ni/NiO electroactive catalytic sites on the GCE surface. Hence, these results suggest that the proposed Ni/NiO@PANI electrochemical sensor is a robust and stable electrode for the nanomolar detection of Ep, which identifies a new class of attractive modified electrodes for chemical sensors.

#### 4. Conclusions

In this research work, to construct a catalytically active Ni/NiO homogeneously impregnated PANI nanoarchitecture as a robust bifunctional catalyst, a combustible redox crystallization followed by oxidative polymerization approach is followed. This obtained potentially desirable bifunctional Ni/NiO@PANI catalyst is showing nanomolar detection ability toward EP with a nanomolar sensitivity of  $0.117 \text{ nA } \mu\text{M}^{-1}$ , detection limit of 0.087 nM and quantification limit values of 0.29 nM, similarly and showing excellent catalytic reduction toward nitro- amino-phenol (4-NP to 4-AP) catalysis within 8 min, which is only composed of nonprecious abundant elements. Hence, the Ni/NiO@PANI hybrid active site with unique core-shell nanoarchitecture, tuned electronic properties, ferromagnetic feature of Ni, anti-corrosion feature of PANI, and synergy between core-shell systems is yielded owing to rational construction of metal/metal oxide/carbon hybrid interfaces (Ni/NiO@PANI), which overcomes significant aggregation, enhanced ion/charge transport and magnetically recovery during catalysis, which holds promise as an excellent bifunctional catalyst. Further functionalization or changes would be essential and responsible for the multi-functional activity, including sensor platform, magnetically recoverable catalyst, and storage devices.

#### CRediT authorship contribution statement

**Manigandan Ramadoss:** Conceptualization, Methodology, Investigation, Software, Validation, Writing - original draft. **Yuanfu Chen:** Supervision, Project administration, Funding acquisition, Writing - review & editing. **Suresh Ranganathan:** Writing - review & editing, Software, Validation. **Krishnan Giribabu:** Formal analysis, Validation. **Dhanasekaran Thangavelu:** Resources, Software. **Padmanaban Annamalai:** Investigation, Resources. **Narayanan Vengidusamy:** Conceptualization, Supervision, Writing - review & editing.

#### Declaration of Competing Interest

The authors declare no conflict of interest.

#### Acknowledgments

The research was supported by the National Natural Science Foundation of China (Grant No. 21773024), Sichuan Science and Technology program (Grant Nos. 2020YJ0324, 2020YJ0262), Reformation and Development Funds for Local Region Universities from China Government in 2020 (Grant Nos. ZCKJ 2020-11) and China Postdoctoral Science Foundation (Grant No. 2019M653376).

## Appendix A. Supplementary data

Supplementary material related to this article can be found, in the online version, at doi:<https://doi.org/10.1016/j.apcata.2021.118028>.

## References

- [1] A. Baba, T. Mannen, Y. Ohdaira, K. Shinbo, K. Kato, F. Kaneko, N. Fukuda, H. Ushijima, *Langmuir: ACS J. Surf. Colloid.* 26 (2010) 18476–18482.
- [2] T. Dhanasekaran, R. Manigandan, A. Padmanaban, R. Suresh, K. Giribabu, V. Narayanan, *Sci. Rep.* 9 (2019) 13250.
- [3] X. Liu, M. Bauer, H. Bertagnolli, E. Roduner, J. van Slageren, F. Philipp, *Phys. Rev. Lett.* 97 (25) (2006), 253401.
- [4] Y. Hu, B. Yu, M. Ramadoss, W. Li, D. Yang, B. Wang, Y. Chen, *ACS Sustain. Chem. Eng.* 7 (2019) 10016–10024.
- [5] W. Tang, L. Li, X. Zeng, *Talanta* 131 (2015) 417–423, 6.
- [6] J. Sochr, L. Švorc, M. Rievaj, D. Bustin, *Diamond Relat. Mater.* 43 (2014) 5–11.
- [7] X. Liu, L. Dai, *Nat. Rev. Mater.* 1 (2016) 16064–16076.
- [8] J. Huang, S. Virji, B.H. Weiller, R.B. Kaner, *Chem. Eur. J.* 10 (2004) 1314–1319.
- [9] Y. Guo, T. Wang, F. Chen, X. Sun, X. Li, Z. Yu, P. Wan, X. Chen, *Nanoscale* 8 (2016) 12073–12080.
- [10] P. Prabhu, R. Suresh Babu, S. Sriman Narayanan, *Sens. Actuators B: Chem.* 156 (2011) 606–614.
- [11] B. Wang, Y. Hu, B. Yu, X. Zhang, D. Yang, Y. Chen, *J. Power Sources* 433 (2019), 126688.
- [12] A. Padmanaban, N. Padmanathan, T. Dhanasekaran, R. Manigandan, S. Srinandhini, P. Sivaprakash, S. Arumugam, V. Narayanan, *J. Electroanal. Chem.* 877 (2020), 114658.
- [13] X. Wang, J. He, B. Yu, B. Sun, D. Yang, X. Zhang, Q. Zhang, W. Zhang, L. Gu, Y. Chen, *Appl. Catal. B: Environ.* 258 (2019), 117996.
- [14] X. Wang, Y. Chen, J. He, B. Yu, B. Wang, X. Zhang, W. Li, M. Ramadoss, W. Zhang, D. Yang, *ACS Appl. Energy Mater.* 3 (2019) 1027.
- [15] K. Sanjeev Kumar, K. Giribabu, R. Suresh, R. Manigandan, S. Praveen Kumar, V. Narayanan, *Mater. Lett.* 283 (2021), 128804.
- [16] Y. Hu, B. Yu, W. Li, M. Ramadoss, Y. Chen, *Nanoscale* 11 (2019) 4876–4884.
- [17] W. Tang, L. Li, X. Zeng, *Talanta* 131 (2015) 417–423.
- [18] S.P. Kumar, K. Giribabu, R. Manigandan, S. Munusamy, S. Muthamizh, A. Padmanaban, T. Dhanasekaran, R. Suresh, V. Narayanan, *Electrochim. Acta* 194 (2016) 116–126.
- [19] M. Tyagi, M. Tomar, V. Gupta, *Biosens. Bioelectron.* 52 (2014) 196–201.
- [20] J. He, Y. Chen, W. Lv, K. Wen, C. Xu, W. Zhang, Y. Li, W. Qin, W. He, *ACS Nano* 10 (2016) 10981–10987.
- [21] M.A. Pandit, D. Sai Hemanth Kumar, S. Billakanti, M. Ramadoss, K. Muralidharan, *J. Phys. Chem. C* 124 (2020) 18010–18019.
- [22] K. Giribabu, S.Y. Oh, R. Suresh, S.P. Kumar, R. Manigandan, S. Munusamy, G. Gnanamoorthy, J.Y. Kim, Y.S. Huh, V. Narayanan, *Microchim. Acta* 183 (2016) 2421–2430.
- [23] N. Saraf, E.R. Woods, M. Pepler, S. Seal, *Biosens. Bioelectron.* 117 (2018) 40–46.
- [24] R. Manigandan, T. Dhanasekaran, A. Padmanaban, K. Giribabu, R. Suresh, V. Narayanan, *Nanoscale Adv.* 1 (2019) 1531–1540, h.
- [25] M.Y. Emran, M. Mekawy, N. Akhtar, M.A. Shenashen, I.M. El-Sewify, A. Faheem, S. A. El-Safty, *Biosens. Bioelectron.* 100 (2018) 122–131.
- [26] R.N. Goyal, S. Bishnoi, *Talanta* 84 (2011) 78–83.
- [27] Y. Furukawa, F. Ueda, Y. Hyodo, I. Harada, T. Nakajima, T. Kawagoe, *Macromolecules* 21 (1988) 1297–1305.
- [28] R. Suresh, K. Giribabu, R. Manigandan, S.P. Kumar, S. Munusamy, S. Muthamizh, V. Narayanan, *Syn. Metals* 196 (2014) 151–157.
- [29] V.K. Harika, H.K. Sadhanala, I. Perelshtein, A. Gedanken, *Ultrason. Sonochem.* 60 (2020), 104804.
- [30] M. Ramadoss, Y. Chen, Y. Hu, W. Li, B. Wang, X. Zhang, X. Wang, B. Yu, *J. Power Sources* 451 (2020), 227753.
- [31] M. Ramadoss, Y. Chen, Y. Hu, B. Wang, J. Ramkumar, M. Karpuraranjith, X. Wang, D. Yang, *J. Mater. Sci. Tech.* 78 (2021) 229–237.
- [32] H. Singh, R. Yadav, P. Rajput, D. Bhattacharyya, S.N. Jha, A.K. Sinha, *Energy Fuels* 33 (2019) 5332–5342.
- [33] R. Suresh, K. Giribabu, R. Manigandan, A. Stephen, V. Narayanan, *Mater. Lett.* 128 (2014) 369–372.
- [34] K. Mallick, M. Witcomb, M. Scurrill, A. Strydom, *Chem. Phys. Lett.* 494 (2010) 232–236.
- [35] M. Karpuraranjith, Y. Chen, X. Wang, B. Yu, S. Rajaboopathi, D. Yang, *Appl. Surf. Sci.* 507 (2020), 145026.
- [36] P. Thivya, J. Wilson, *Microchem. J.* 145 (2019) 883–891.
- [37] W. Zhang, Y. Sun, L. Zhang, *Ind. Eng. Chem. Res.* 54 (2015) 6480–6488.
- [38] N. Tavakkoli, N. Soltani, F. Shahdost-Fard, M. Ramezani, H. Salavati, M.R. Jalali, *Mikrochim. Acta* 185 (2018) 479.
- [39] J. Jang, J. Ha, J. Cho, *Adv. Mater.* 19 (2007) 1772–1775.
- [40] J. Zhang, D. Wang, Y. Li, *ACS Appl. Mater. Interfaces* 1 (2019) 13557–13563.
- [41] M. Ramadoss, Y. Chen, Y. Hu, D. Yang, *Electrochim. Acta* 321 (2019) 134666.
- [42] L. Srisombat, J. Nonkumwong, K. Suwannarat, B. Kuntalae, S. Ananta, *Colloids Surf. A Physicochem. Eng. Asp.* 512 (2017) 17–25.
- [43] R. Suresh, K. Giribabu, R. Manigandan, S.P. Kumar, S. Munusamy, S. Muthamizh, A. Stephen, V. Narayanan, *Sens. Actuators B: Chem.* 202 (2014) 440–447.
- [44] B. Wang, Y. Chen, Q. Wu, Y. Lu, X. Zhang, X. Wang, B. Yu, D. Yang, W. Zhang, *J. Mater. Sci. Technol.* 74 (2021) 11–20.
- [45] X. Zhu, Y. Chen, C. Feng, W. Wang, B. Bo, R. Ren, G. Li, *Anal. Chem.* 897 (2017) 4131–4138.